# Disordered Structure and Structural Water Promote Aqueous Sodium-ion Energy Storage in Na<sub>0.27</sub>MnO<sub>2</sub> Birnessite

Xiaoqiang Shan<sup>a</sup>, Fenghua Guo<sup>a</sup>, Daniel S. Charles<sup>a</sup>, Zachary Lebens-Higgins<sup>b</sup>, Sara Abdel Razek<sup>b</sup>, Jinpeng Wu<sup>c</sup>, Wenqian Xu<sup>d</sup>, Wanli Yang<sup>c</sup>, Katharine L. Page<sup>e</sup>, Jorge C. Neuefeind<sup>e</sup>, Mikhail Feygenson<sup>e, f</sup>, Louis F. J. Piper<sup>b</sup>, Xiaowei Teng<sup>\*a</sup>

Corresponding author: Xiaowei Teng\*

E-mail address: xw.teng@unh.edu

#### **Abstract**

Birnessite is a low-cost and environmentally friendly layered material for aqueous electrochemical energy storage; however, its storage capacity is poor, mainly due to its narrow potential window in an aqueous electrolyte and low redox activity. Herein we reported a Na-rich disordered birnessite structure (Na<sub>0.27</sub>MnO<sub>2</sub>) for aqueous Na-ion electrochemical storage with a much-enhanced storage capacity and cycling life (83 mAh g<sup>-1</sup> after 5000 cycles in full-cell). Neutron total scattering and *in situ* X-ray diffraction measurements showed that both structural water and the Na-rich disordered structure attributed to the improved electrochemical performance of Na<sub>0.27</sub>MnO<sub>2</sub>. Particularly, the co-deintercalation of the hydrated water and Na-ion during the high potential charging process resulted in the shrinkage of interlayer distance and thus stabilized the layered structure. Our results provide a genuine insight into how structural disordering and structural water improve Na-ion storage in a layered electrode and open up a new exciting direction for improving aqueous batteries.

<sup>&</sup>lt;sup>a</sup>Department of Chemical Engineering, University of New Hampshire, Durham, New Hampshire 03824, USA

<sup>&</sup>lt;sup>b</sup>Department of Physics, Applied Physics and Astronomy, Binghamton University, Binghamton, New York 13902, United States

<sup>&</sup>lt;sup>c</sup>Advanced Light Source, Lawrence Berkeley National Laboratory, Berkeley, California 94720, USA

<sup>&</sup>lt;sup>d</sup>Advanced Photon Source, Argonne National Laboratory, Argonne, Illinois 60439, USA

<sup>&</sup>lt;sup>e</sup>Chemical and Engineering Materials Division, Spallation Neutron Source, Oak Ridge National Laboratory, Oak Ridge, Tennessee 37831, USA

<sup>&</sup>lt;sup>f</sup>Juelich Centre for Neutron Science, Forschungszentrum Juelich GmbH, 52425 Juelich, Germany

Developing electrochemical energy storage (EES) technologies using safe and earth-abundant materials has become increasingly attractive for economically storing electric energy generated by solar and wind. Aqueous EES devices using sodium (Na)-ions as charge carriers are promising alternatives to non-aqueous lithium (Li)-ion batteries (LIBs) owing to their low cost, high safety and the availability of Na sources in terrestrial reserves. However, the storage of Na-ion is challenging because of its large ionic radius. Consequently, LIB host materials (especially cathode materials) that typically have a close-packed array of oxide ions may not be able to reversibly accommodate insertion and extraction of the Na-ions.

Two design principles have been used to tackle the intercalation of Na-ion. One is the replacement of oxygen anions (O<sup>2-</sup>) with anions that have weaker bonding with metal cations so that cations are sufficiently mobile in the electrode. Recent studies show promise of hexacyano ion  $(C \equiv N)_6^{6-}$  based electrode materials for Na- and potassium (K)-ion storage due to the weakened bonding between cyanide (C≡N)<sup>-</sup> and cations. Cui's group demonstrated that potassium copper hexacyanoferrate and its analogues can function as stable electrode materials for aqueous K- and Na-ion storage.<sup>3-6</sup> Sodium manganese hexacyanoferrate reported by Goodenough's group showed good energy performance and cycling life in a non-aqueous electrolyte. 7-9 Another approach is to use a large interstitial host framework, especially layered structure, for Na-ion storage. These layered materials with planar or zigzag layers show different polymorphs (P2, P3 or O3 symmetry) with respect to the sites of the intercalated alkali ions by simply altering the stacking of transition metal-oxygen octahedra ([MO<sub>6</sub>]). Pioneer works on studying Na-ion intercalation in layered Na<sub>x</sub>MnO<sub>2</sub> were reported by Hagenmuller in the 1980s. 13,14 However, the mechanistic understanding of Na-ion storage inside various host materials is still far from settled. This is largely due to the large size of Na-ions compared with Li-ions, which give rise to different intercalation chemistry between Na-ions and Li-ions, 15 so that the fundamental understanding obtained from Li-ion storage may not be directly applied in the Na-ion electrodes. <sup>16-19</sup> In addition, layered metal oxides especially LiNi<sub>1-x-y</sub>Co<sub>x</sub>Mn<sub>y</sub>O<sub>2</sub> (NCM) cathode materials suffer from an abrupt c-lattice collapse (up to 5%) at high potential charging state, resulting in the pulverization of active materials and thus degradation of the performance.

Birnessite (δ-MnO<sub>2</sub>) is a layered structure comprised of two-dimensional sheets of edge-shared MnO<sub>6</sub> octahedra with intercalated cations and/or water between interlayer.<sup>20-24</sup> Even though birnessite has a rather large interlayer distance (~ 7 Å), its storage capacities for Na-ion in aqueous electrolytes were typically low, mainly due to the limited thermodynamically stable potential window (~ 1.2 V) of an aqueous electrolyte and ineffective redox process.<sup>25-27</sup> Recent studies showed that a concentrated Libis(trifluoromethane sulfonyl)imide salt in water (water-in-salt) electrolyte helped the formation of an electrode-electrolyte interphase on a Mo<sub>6</sub>S<sub>8</sub> anode that prevented the direct contact between anode and water, and thus achieved potential window of 3.0 V for aqueous EES without gas evolution reactions.<sup>28</sup> A similar wide potential window was reported for aqueous electrolyte using hydrate-melt of Li salts. 29,30 However, little work has been reported to date on how to widen the potential window of birnessite electrode materials in aqueous electrolytes. Here we present an effective strategy to significantly improve the discharge capacity and cycle life of birnessite (full cell capacity of 83 mAh g<sup>-1</sup> at 1 A g<sup>-1</sup> after 5000 cycles) through increasing the stable potential window and promoting redox charge transfer process towards aqueous Na-ion storage. Our results demonstrated that Na-rich and disordered birnessite structure can afford a stable potential window of 2.5 V in an aqueous electrolyte with high overpotential towards the gas evolution reactions. Moreover, co-deintercalation of water molecules along with Na-ion at the high potential charging process, evidenced by in situ XRD measurement, could stabilize the layered structure from over-expansion of the interlayer distance.

#### Structural characterizations and formation mechanism

Different from wet chemistry methods to synthesize birnessite materials with a limited amount of pre-intercalated Na-ions, <sup>23,24,26,31</sup> in this study disordered and Na-rich birnessite were prepared at 270 °C in air via a solid-state reaction between NaOH and Mn<sub>3</sub>O<sub>4</sub> nanoparticles (Mn<sub>3</sub>O<sub>4</sub> particles were synthesized using a method reported previously<sup>32</sup>). By altering the molar ratios between NaOH and Mn<sub>3</sub>O<sub>4</sub>, various sodium-intercalated manganese oxides (Na<sub>δ</sub>MnO<sub>x</sub>; δ: 0.10, 0.17 and 0.27) were prepared, verified by inductively coupled plasma mass spectrometry (ICP-MS) measurements (Table S1). The atomic ratio of Na/Mn remained around 0.27 even when a higher NaOH/Mn<sub>3</sub>O<sub>4</sub> ratio of 4 was used (Figure S1). The Na/Mn ratio of 0.27 is considerably higher than that of birnessite materials previously reported for aqueous energy storage, though several Na-rich birnessite materials have also been reported in non-aqueous Na-ion storage (Table S2).<sup>20-24</sup> Figure 1a and Figure S2 show that as Na concentrations increased from 0.10 to 0.27, the morphologies of resulting Na-Mn-O materials evolved from a mixture of faceted particles and planar structures to a complete planar structure. The atomic ordering of the resulting Na-Mn-O materials was analyzed using neutron total scattering and the atomic pair distribution function (PDF) (Figure 1b), from which both the Bragg and diffusive scattering were analyzed to provide local structural details such as defects, mismatch or disorder at the atomic level. The structural parameters of various Na<sub>5</sub>MnO<sub>x</sub> materials obtained from refinement are summarized in Figure S3 and Table S3-S6. The neutron PDF showed that the coherent length of Na<sub>8</sub>MnO<sub>x</sub> materials (a distance at which the peaks of atomic pairs vanished) decreased from > 50 Å to  $\sim 30 \text{ Å}$  as Na content ( $\delta$ ) increases, indicating more confined crystalline order. Namely, Na<sub>δ</sub>MnO<sub>x</sub> materials cannot sustain long-range crystallinity and became more disordered when more Naions are incorporated into the structure. Figure 1c shows that as Na concentration (δ) increased, Na<sub>δ</sub>MnO<sub>x</sub> materials showed pure phase  $Mn_5O_8$  ( $\delta = 0$ ), mixture of  $Mn_5O_8$  and layered  $MnO_2$  ( $\delta = 0.10$  and 0.17). When  $\delta$  reached 0.27, a pure triclinic birnessite structure formed an interplanar distance of 7.14 Å. The chemical formula was determined to be Na<sub>0.27</sub>MnO<sub>2</sub>·0.63H<sub>2</sub>O, where the Na cations and structural water molecules (determined from thermal gravimetric analysis shown in Figure S5) occupied the interlayer regions.

Neutron PDF studies shown in Figure 2 demonstrate the evolution of the local structure at the atomic level during the phase transition from Mn<sub>3</sub>O<sub>4</sub> to Mn<sub>5</sub>O<sub>8</sub>, and finally to MnO<sub>2</sub> birnessite. The PDF data were normalized by the intensity of the peak at 1.9 Å to see the comparative changes of the structural details as  $\delta$  increased, and the original coherent scattering and structure factor data can be found in Figure S6. The peaks of PDF can be indexed as O-H pair (0.95 Å, P1) from water (a), one Mn-O pair (1.9 Å, P2) from the [MnO<sub>6</sub>] octahedral unit and another Mn–O pair (2.2 Å, P3) from Mn atoms in prismatic sites, Mn-Mn or O-O pair (2.8 Å, P4), and Mn-O pair (3.5 Å, P5) from the nearest neighbors of [MnO<sub>6</sub>] octahedral units, respectively. The contribution of individual pairs such as Mn-O, Mn-Mn, O-O, and Mn-Na, to the overall PDF of the materials can be found in Figure S7. It is notable that O-H pair (P1) and Mn-O pairs (P2, P3, P5, and P7) showed negative peaks due to negative coherent neutron scattering lengths of H and Mn atoms (-3.74 and -3.73 femtometer, respectively). The Mn-O pair (1.9 Å, P2) is attributed to Mn-O octahedral coordination in both Mn<sub>5</sub>O<sub>8</sub> (b) and layered Na<sub>0.27</sub>MnO<sub>2</sub> (c) structures. The Mn-O pair (2.2 Å, P3) is attributed to Mn(II)-O from Mn<sub>5</sub>O<sub>8</sub> phase (d), which decreased relatively to Mn(IV)-O pair at P2 as δ increased, congruent with the decreasing phase fractions of Mn<sub>5</sub>O<sub>8</sub>. The positive peaks at 2.8 Å (P4) are attributed to Mn–Mn or O–O bonding from adjacent [MnO<sub>6</sub>] octahedral units in Mn<sub>5</sub>O<sub>8</sub> (e) and  $Na_{0.27}MnO_2$  (f) relative to the Mn(IV)–O pair, which did not change significantly as  $\delta$  increased. A similar trend can be found in the Mn-O pair at 3.5 Å (P5) from adjacent [MnO<sub>6</sub>] in Mn<sub>5</sub>O<sub>8</sub> (g) and Na<sub>0.27</sub>MnO<sub>2</sub> phases (h). The peaks at  $\sim 4.0$  Å (P6 and P7) showed a rather interesting transition from the positive to negative direction as δ increased. The positive peak at 3.96 Å (P6) is related to O-O pairs (i) in Mn<sub>5</sub>O<sub>8</sub> either within the same [Mn(IV)O<sub>6</sub>] octahedral unit or [Mn(II)–O] units where Mn<sup>2+</sup> is located in the trigonal prismatic site. In contrast, the negative peak at 4.0 Å (P7) is attributed to Mn–Na pair at 4.11Å (h) from the interaction between Na-ions in the interlayer and Mn<sup>4+</sup> from [MnO<sub>6</sub>] octahedral unit or Mn-O<sub>w</sub> pair (O<sub>w</sub> from structural water in the interlaver) at 3.73 Å (h) from the interaction between H<sub>2</sub>O in the interlaver and Mn<sup>4+</sup>, both from Na<sub>0.27</sub>MnO<sub>2</sub> layered phase. The interplay between negative peaks of Mn–Na and Mn–O<sub>W</sub> pairs in the Na<sub>0.27</sub>MnO<sub>2</sub> phase and the positive peak of O-O pair in Mn<sub>5</sub>O<sub>8</sub> phase at around 4.0 Å explains

the overall peak change from the positive to negative direction when  $\delta$  increased. This suggests again that the phase transition from  $Mn_5O_8$  to  $Na_{0.27}MnO_2$  birnessite was driven by Na-ion insertion during the solid-state annealing.

Based on the above neutron PDF analysis and in-situ XRD during the thermal treatment (Figure S8), a formation mechanism of Na<sub>0.27</sub>MnO<sub>2</sub> birnessite is proposed in Figure 3. Basically, Mn<sub>3</sub>O<sub>4</sub> nanoparticles were first converted into Mn<sub>5</sub>O<sub>8</sub> materials through oxidation of [Mn(III)O<sub>6</sub>] octahedra of Mn<sub>3</sub>O<sub>4</sub> into [Mn (IV)O<sub>6</sub>] units, followed by Na-ion driven conversion from Mn<sub>5</sub>O<sub>8</sub> to Na<sub>0.27</sub>MnO<sub>2</sub> birnessite during the thermal annealing in air. It is notable that Mn<sub>5</sub>O<sub>8</sub> and Na<sub>0.27</sub>MnO<sub>2</sub> share similar structural characteristics.  $Mn_5O_8$  has a layered structure and consists of sheets of  $[Mn_3^{4+}O_8]^{4-}$  in the bc plane. It is apparent that the  $[Mn_3^{4+}O_8]^{4-}$  sheets resemble the structure of  $Na_{0.27}MnO_2$  birnessite comprised of infinite [MnO<sub>6</sub>] octahedral layers with intercalated Na cations in between. The transition from Mn<sub>5</sub>O<sub>8</sub> to  $Na_{0.27}MnO_2$  birnessite is an equivalent process to the ion-exchange of  $Mn^{2+}$  ions in the  $Mn_2^{2+}Mn_3^{4+}O_8$  with  $Na^+$  ions in the solid state. Our result suggests that the  $Mn^{2+}$  ions with trigonal prismatic coordination located between the interlayer of Mn<sub>5</sub>O<sub>8</sub> have a higher mobility than octahedrally coordinated Mn<sup>4+</sup> ions. Therefore, insertion of Na-ions into the Mn<sup>2+</sup> site was kinetically favored, accompanied by the oxidation of Mn<sup>2+</sup> ions into Mn<sup>4+</sup> during the migration of Mn<sup>2+</sup> to the [Mn<sup>4+</sup><sub>3</sub>O<sub>8</sub>]<sup>4-</sup> layers, and drove the formation of Na<sub>0.27</sub>MnO<sub>2</sub>. XRD showed that anhydrous Na<sub>0.27</sub>MnO<sub>2</sub> has an interlayer distance of 5.58 Å (Figure S9), very similar to that of Mn<sub>5</sub>O<sub>8</sub> (5.2 Å). Upon water intercalation, the resulting Na<sub>0.27</sub>MnO<sub>2</sub>·0.63H<sub>2</sub>O showed an increased interlayer distance of 7.14 Å.33 The Na-ion driven conversion from Mn<sub>5</sub>O<sub>8</sub> to Na<sub>0.27</sub>MnO<sub>2</sub> reported here contrasts the formation of Li-MnO<sub>2</sub> via the ion-exchange between Ca<sub>2</sub>Mn<sub>3</sub>O<sub>8</sub> (Ca<sup>2+</sup><sub>2</sub>Mn<sup>4+</sup><sub>3</sub>O<sub>8</sub>), isomorphic structure of Mn<sub>5</sub>O<sub>8</sub> (Mn<sup>2+</sup><sub>2</sub>Mn<sup>4+</sup><sub>3</sub>O<sub>8</sub>), and molten lithium nitrate reported by Doeff's group.<sup>34</sup> In the formation of Li-MnO<sub>2</sub>, Li-ions occupied all the available octahedral sites between the [Mn<sub>3</sub><sup>4+</sup>O<sub>8</sub>]<sup>4-</sup> layers rather than the trigonal prismatic sites occupied by Ca<sup>2+</sup> in the parent Ca<sub>2</sub>Mn<sub>3</sub>O<sub>8</sub> compound due to much smaller size of Li<sup>+</sup> compared with Ca<sup>2+</sup>, resulting in the complete conversion to layered LiMnO<sub>2</sub> with R3m or O3 symmetry.

#### **Electrochemical properties**

Electrochemical performance of various  $Na_\delta MnO_x$  materials was tested in a 0.1 M  $Na_2SO_4$  electrolyte in a three–electrode half–cell using cyclic voltammetry (CV) measurements between –1.25 V to 1.25 V (vs Ag/AgCl) at scan rates ranging from 5 to 1000 mV s<sup>-1</sup> (Figure S10). Figure 4a shows the CVs of disordered Na-rich  $Na_{0.27}MnO_2$ , where distinct redox peaks can be observed at all the tested scan rates. As shown in Figure 4b, the  $Na_{0.27}MnO_2$  material exhibits higher specific capacities compared with other  $Na_\delta MnO_x$  materials at all scan rates, with a maximum capacity of 147 mAh  $g^{-1}$  at a scan rate of 5 mV s<sup>-1</sup>. Figure 4a shows that when scan rates increased from 5 to 1000 mV s<sup>-1</sup>,  $Na_{0.27}MnO_2$  shows a small peak shift in the anodic process from 0.78 V to 1.00 V and peak shift in the cathodic process from 0.12 V to – 0.17 V, compared with the other  $Na_\delta MnO_x$  materials shown in Figure S11. This indicates Na-ion transport in  $Na_{0.27}MnO_2$  required a lower overpotential at higher charging rates. Further quantitative evaluation of Na-ion transport in all  $Na_\delta MnO_x$  materials was obtained using a current–pulse relaxation method. As shown in Figure S12, the  $Na_{0.27}MnO_2$  material showed a diffusion coefficient of 38.7 relative to  $Mn_5O_8$ , much higher than the other  $Na_\delta MnO_x$  materials. This result was again congruent with CV data, where  $Na_{0.27}MnO_2$  had the lowest energy barrier for Na-ion intercalation since it had a more dominant phase of layered birnessite than other  $Na_\delta MnO_x$  materials that were a mixture of birnessite and  $Mn_5O_8$ .

Figure S13 shows X-ray photoelectron spectroscopy (XPS) spectra of  $Na_{0.27}MnO_2$  materials at pristine, charged and discharged states. The pristine state Mn showed a dominant Mn<sup>4+</sup> state with characteristic Mn  $2p_{1/2}$  and Mn  $2p_{3/2}$  features at 654.2 eV and 642.5 eV, and less distinct but discernable Mn<sup>3+</sup> features at 642.2 eV and 653.3 eV, respectively (Figure S14). The ratio between Mn<sup>4+</sup> and Mn<sup>3+</sup> was calculated to be 0.72:0.28. Since the Mn<sup>3+</sup> resulted from the intercalated Na-ion in interlayers of MnO<sub>2</sub>, a

 $Mn^{4+}/Mn^{3+}$  ratio of 0.72:0.28 suggested a Na/Mn ratio of 0.28, nearly identical to the ICP-MS result (Na:Mn = 0.27). At charged state (1.25 V)  $Na_{0.27}MnO_2$  showed a  $Mn^{4+}/Mn^{3+}$  ratio of 0.97:0.03, and a  $Mn^{4+}/Mn^{3+}$  ratio of 0.62:0.38 at discharged state (-1.25 V). Although the exact determination of  $Mn^{2+/3+/4+}$  ratio can be challenging from the Mn 2p core region due to the multiplet structure and significant overlap between different oxidation states, XPS results confirmed that  $Na_{0.27}MnO_2$  materials had a  $Mn^{4+}/Mn^{3+}$  redox couple during insertion and extraction of Na-ions.

To further understand the charge-transfer process of  $Na_{0.27}MnO_2$  material, electro–kinetic analysis was conducted, from which the distribution of the diffusion–limited redox and surface–controlled capacitive charge transfer processes was determined through analyzing the current (i) at different scan rates (v) at a given potential. Assuming that the total current (i) at a particular potential contains both capacitive current ( $i_1$ = $k_1$ v) and diffusion–limited redox current ( $i_2$ = $k_2$ v<sup>1/2</sup>):<sup>35</sup>

$$i = i_1 + i_2 = k_1 v + k_2 v^{1/2}$$
 or  $i/v^{1/2} = k_1 v^{1/2} + k_2$ 

The values of  $k_1$  and  $k_2$  can be determined by plotting  $i/v^{1/2}$  as a function of  $v^{1/2}$ , and therefore the relative current response from the capacitive process and/or diffusion–limited redox process at a given potential of each scan rate can be obtained. The CVs marked with capacitive and diffusion–limited redox contributions at scan rates ranging from 5 to  $1000 \text{ mV s}^{-1}$  can be found in Figure S15, and summarized results are plotted in Figure S16. At a scan rate of 5 mV s<sup>-1</sup> the diffusion-limited redox process contributes to 73% of overall capacity, equivalent to a redox capacity of  $107 \text{ mAh g}^{-1}$  ( $147 \text{ mAh g}^{-1} \times 73\%$ ). This value also corresponded to 0.36 electron transfer per Mn atom (the theoretical capacity of NaMnO2 is  $308 \text{ mAh g}^{-1}$ ), in good agreement with the 0.35 electron transfer between charged and discharge states of Na<sub>0.27</sub>MnO<sub>2</sub> determined by XPS measurements.

Long-term energy and power performance of Na<sub>0.27</sub>MnO<sub>2</sub> material were tested in symmetric fullcells for 5,000 galvanostatic cycles in a potential window of 2.5 V. Toray paper was used as the current collector, which was stable during the measurements without causing gas evolution reactions (Figure S17). Figure 4c and Figure S18 show that voltage-capacity profiles are nearly linear at all the tested current densities ranging from 1 to 10 A g<sup>-1</sup>, pointing to a single-phase solid solution redox reaction. Accordingly, the electrode capacities were calculated to be 83 mAh g<sup>-1</sup> to 24 mAh g<sup>-1</sup> at corresponding discharge times ranging from 160 s (a C-rate of 23) to 4.5 s (a C-rate of 800). Moreover, Na<sub>0.27</sub>MnO<sub>2</sub> material exhibits an excellent cycle stability up to 5000 cycles without obvious capacity loss, as well as nearly 100% coulombic efficiency and high energy efficiency at various current densities (Figure 4d, 4e). The Ragone plot in Figure 4f compares the energy and power performance of Na<sub>0.27</sub>MnO<sub>2</sub> materials with several aqueous or nonaqueous EES devices, including Panasonic (17500) Li-ion battery, <sup>36</sup> α-MnO<sub>2</sub>, δ-MnO<sub>2</sub> or amorphous birnessites, <sup>31,37-39</sup> and tunnel-structured Na<sub>0.44</sub>MnO<sub>2</sub> and O3 type NaMnO<sub>2</sub>. <sup>40,41</sup> It is clear that the reported Na<sub>0.27</sub>MnO<sub>2</sub> systems had a comparable and/or superior performance even compared with non-aqueous Naion EES systems. It is more important to point out that often reported performances of EES are for tests with limited cycling numbers (usually from 100 to 2000), while our data shown in Figure 4f were after 5000 cycles. We also compared our electrochemical performance with other Mn-based electrode materials in aqueous storage (Table S7), <sup>37,40-43</sup> showing that Na<sub>0.27</sub>MnO<sub>2</sub> is among the best electrode materials in term of the energy, rate and cycling performance for aqueous Na-ion storage. It is also worth mentioning that in full-cell tests Na<sub>0.27</sub>MnO<sub>2</sub> materials showed continuously increasing capacities during the initial cycling especially at the low current densities. The electrochemical impedance spectroscopy measurements shown in Figure S19 demonstrate decreasing solution resistance during the initial electrochemical cycling, congruent with I-R drop in the discharge curves (Figure S20). Therefore, it suggested that the increasing capacities in early charge and discharge cycles can be attributed to the slow building-up of an ionic interface during the initial cycling before the electrode reached its best electrochemical condition. Similar behaviours were observed in Mn<sub>5</sub>O<sub>8</sub> materials for aqueous Na-ion storage reported previously, and were also observed in several non-aqueous systems such as Na-S, Na<sub>0.67</sub>Ni<sub>1/6</sub>Co<sub>1/6</sub>Mn<sub>2/3</sub>O<sub>2</sub> cathode, and LiFe<sub>0.9</sub>P<sub>0.95</sub>O<sub>4</sub> cathode.44-46

## Water co-deintercalation during high potential charging

*In-situ* XRD measurements were conducted along with the CV test at a scan rate of 0.75 mV s<sup>-1</sup> as shown in (Figure S21), where diffraction peaks at the  $2\theta$  angles of  $\sim 5.8^{\circ}$  and  $\sim 29^{\circ}$  can be attributed to (001) basal diffraction peak and (020) Bragg, respectively. As shown in Figure 5, when the potential increased from -1.25 V to 1.25 V (charging process), the (001) peak shifted to a lower 2θ angle, corresponding to an increasing interlayer distance of (001) plane  $(d_{001})$  because the electrostatic repulsion between the [MnO<sub>6</sub>] layers leads to an increase in the interlayer spacing upon the removal of the positive Na-ions, whereas (020) Bragg peak shifted to a higher 2θ angle simultaneously with a decreasing d<sub>020</sub> due to the increased fraction of Mn<sup>4+</sup> ions that have a smaller ionic radius than Mn<sup>3+</sup>. During the reduction process (from 1.25 V to -1.25 V), (001) and (020) diffraction peaks were restored to the original states. Nearly identical behaviors were also found in the second cycle. Na<sub>0.27</sub>MnO<sub>2</sub> material showed a 4.4% change in the d<sub>001</sub> spacing of (from 7.33 Å to 7.02 Å) between fully charged and discharged states, more significant than previously reported MnO<sub>2</sub> birnessite (1.7%) with a potential window of 1.2 V and a low capacity of 36 mAh g<sup>-1</sup>.<sup>26</sup> The contour plot in Figure 5 reflects peak shifts of the (001) basal diffraction peak of Na<sub>0.27</sub>MnO<sub>2</sub> during charging and discharging process. The observed continuous and reversible peak shifting without a staged structural transformation indicates high structural stability of Na<sub>0.27</sub>MnO<sub>2</sub> during the charging and discharging processes, which explains the good cycle life of Na<sub>0.27</sub>MnO<sub>2</sub> materials.

Moreover, in situ XRD also revealed water trafficking, for the first time, along with Na-ions insertion and extraction during the charging and discharging process. Figure 6 showed that when the potential increased from -1.250 V to -0.106 V, d<sub>001</sub> and the corresponding electrochemical current remained relatively constant, suggesting a non-Faradaic capacitive charge storage process (electrochemical desorption of Na-ions from the surface of the electrode) without involving the extraction of Na-ions from the interlayer region. When the potential increased from -0.106 V to 0.914 V, d<sub>001</sub> increased rapidly from 7.02 Å to 7.33 Å, indicating a large amount of Na-ions were extracted from the interlayer region, concurrent with the increasing Faradaic current; as the potential continuously increased from 0.914 V to 1.25 V, d<sub>001</sub> decreased from 7.33 Å to 7.30 Å. Such a compression of interlayer distance at the higher potential range is likely attributed to the removal of structural water along with the extraction of Na-ions from the interlayer region since a mere Na-ion removal alone would only cause an increase in d<sub>001</sub>. It is important to point out that such compression at high potential only happened in the interlayer distance (along c-direction) because d<sub>020</sub> decreased continuously indicating continued oxidation of Mn<sup>3+</sup> into Mn<sup>4+</sup> when the potential increased from -0.106 V to 1.25 V. Although it is possible that when the potential increased from -0.106 V to 0.914 V the extracted Na-ions would also bring structural water out of the interlayer region, it was obvious that weakened electro-static interaction caused by the Na-ion removal offsets the water removal effect if any, so that the overall interlayer distance still significantly increases. This means that extracted Na-ions at lower anodic potential range (from -0.106 V to 0.914V) brought much less (or none) hydrated water molecules out of the interlayer region compared with the ones extracted at higher anodic potential (from 0.914 V to 1.25 V). In other words, hydrated Na-ions required higher electrical energy to be removed from interlayer region than less hydrated ones. Likewise, during the reduction process as the potential decreased from 1.25 V to 0.951 V, d<sub>001</sub> slightly increased from 7.30 Å to 7.33 Å, and then sharply decreased from 7.33 Å to 7.02 Å as the potential continued to decrease from 0.951 V to -0.682 V. This suggests that inserted Na-ions in the higher cathodic potential range (from 1.25 V to 0.951V) brought more hydrated Naions into the interlayer region compared with ones inserted at lower anodic potentials (from 0.998 V to -0.682 V). Congruent with the observation of the water trafficing during the anodic scan, fully hydrated Naions preferred to be inserted into the interlayer region than less hydrated ones during the cathodic scan.

In conventional LIB layered oxide cathodes, a decrease in the c-lattice is widely observed at higher degrees of delithiation, even when there is no phase transformation. Recent work on a variety of  $LiNi_{1-x-y}Co_xMn_yO_2$  (NMC) compounds found the onset of this decrease in the c-lattice when around 50-60% lithium has been removed from the structure with limited dependence on Ni, Co, or Mn content. In those LIB cathodes, strong nickel/cobalt-oxygen covalency is expected to facilitate charge transfer from the O 2p

orbitals, decreasing the negative-charge on the oxygen.<sup>49</sup> This effectively weakens electrostatic respulsions between neighboring oxygens across the Li-layer leading to a decrease in the interlayer spacing and thereby a decrease in the c-lattice. Upon relithiation, the c-lattice expands and can symettrically match the collapse observed during delithiation.<sup>48,50</sup> Density functional theory (DFT) calculations have shown this effect occurs for the LiMnO<sub>2</sub> system and may need to be considered for other Mn(IV)-systems.<sup>51</sup>

To investigate whether this model can be extended to birnessite in order to explain the observed interlayer shrinkage during charge, we performed XPS measurements for pristine, rinsed, and charged Na<sub>0.27</sub>MnO<sub>2</sub> in conjunction with DFT calculations, shown in Figure 7. In this case, the charged Na<sub>0.27</sub>MnO<sub>2</sub> is binder-free which allowed for increased sensitivity to the Na<sub>0.27</sub>MnO<sub>2</sub> compound (Figure S22). When charged to 1.25 V, there is a decrease in the intensity of the Na peak due to the removal of Na-ions from the interlayer (Figure 7a). The corresponding valence band XPS measurements display only a slight change in the lineshape of the charged electrode compared to the pristine and rinsed samples likely related to the depopulation of states upon the removal of Na-ions. DFT calculations of the total density of states (TDOS) Na<sub>0.27</sub>MnO<sub>2</sub> system weighted by the x-ray photoionization cross-section<sup>6</sup> match well with the experimental spectra suggesting these calculations can be used to comment on Mn 3d-O 2p covalency (Figure 7b). When looking at the weighted O 2p and Mn 3d partial density of states, we find O 2p states contribute at the top of the valence band (0 eV to 2 eV). At 1486 keV, the Mn 3d photoionization cross-section is over 4x higher than the O 2p state so that in the unweighted DFT calculations the O 2p orbitals are the dominant contribution from 0 to 2 eV (Figure S23), i. e. there is discernable Mn-O covalency in the Na<sub>0.27</sub>MnO<sub>2</sub> so that we may have to consider a decrease in the negative-charge on the oxygen with Na-removal. While this highlights the role Mn-O covalency may play in Na-removal, we believe the water trafficking (codeintercalation with Na-ion) at high potentials remains the primary factor in the observed shrinkage of the interlayer for Na<sub>0.27</sub>MnO<sub>2</sub> for the following reasons. Firstly, compared to the NMC LIB electrodes with an interlayer spacing <3 Å, the Na<sub>0.27</sub>MnO<sub>2</sub> system has an interlayer spacing of 7.1 Å. Thus, the oxygenoxygen interaction between adjacent [MO<sub>6</sub>] layers in birnessite, which is inversely correlated to the square of the interlayer distance ( $\propto \frac{1}{r^2}$  where r is the distance between neighboring oxygen) is relatively weak compared to the NMC compounds. Moreover, the structural water within the interlayer of Na<sub>0.27</sub>MnO<sub>2</sub> birnessite provides a "screening" effect that further weakens the O-O interaction, well described by classic Debye-Huckel theory.

Different from the collapse of c-lattice observed in LIB layered oxide cathodes, where the irreversible lattice collapse shows a detrimental effect on the layered structure of the electrode and thus impairs their full utalization for Li-ion storage, the reversible co-deintercalation of structual water in Na<sub>0.27</sub>MnO<sub>2</sub> benefits Na-ion storage. Notably, repetitive insertion and extraction of cations and thus drastic changes of the interlayer distance during prolonged cycling can cause the degradation of the electrode material. Figure 6 showed that as the c-lattice contracted, the b-lattice continue to decrease (both  $d_{001}$  and d<sub>020</sub> decreased). This indicates that the co-deintercalation of water molecules along with Na-ions stabilzes the layered structure against further expansion of the interlayer distance at higher voltages while sustaining an intensive redox process. To the best of our knowledge, this new safety mechanism has never been reported in aqueous energy storage. Moreover, previous investigations of intercalation cations (e.g., Na<sup>+</sup> and Mg<sup>2+</sup>) in aprotic electrolytes in layered materials have shown that insertion kinetics can be greatly improved when additional water molecules group around the inserted cations, where a water solvation shell partially shields the charge of cations within the cation/water co-intercalation compound. 52-56 In this context, co-deintercalation of water molecules at higher voltage would provide an electrostatic shielding effect to Na-ion, so that hydrated Na-ions have a weaker interaction with lattice oxygen anions to facilitate the transport of Na-ions, and therefore allow a high degree of Na-ion extraction when the Na<sub>0.27</sub>MnO<sub>2</sub> was charged to 1.25 V.

## The disordered structure widens the voltage window

Notably, Na<sub>0.27</sub>MnO<sub>2</sub> materials showed an expanded aqueous voltage window of 2.5 V without significant gas evolution reactions, allowing for more energetic Mn<sup>3+</sup>/Mn<sup>4+</sup> redox couples to deliver higher energy and power densities. Although Mn<sub>5</sub>O<sub>8</sub> and Na<sub>0.27</sub>MnO<sub>2</sub> materials showed a 2.5 V stable voltage window for aqueous Na-ion storage (Figure S10, S24), the mechanisms underlying their high resistance toward HER and OER were completely different. Figure 8a shows that O-K sXAS spectra of Na<sub>0.27</sub>MnO<sub>2</sub> and Mn<sub>5</sub>O<sub>8</sub> have similar sharp features below 534 eV from the hybridization between the O-2p band and Mn-3d states. However, only the Mn<sub>5</sub>O<sub>8</sub> material showed distinct fingerprint water-features at the 535 and 537 eV, indicating the formation of a highly ordered hydroxylated interphase on the surface as we reported previously.<sup>43</sup> To understand whether the disordered structure plays a role in mitigating the water decomposition, we synthesized ordered Na<sub>0.19</sub>MnO<sub>2</sub> birnessite via thermal decomposition of NaMnO<sub>4</sub> materials at 800 °C and conducted the Tafel analysis for hydrogen evolution reaction (HER) and oxygen evolution reaction (OER) on disordered Na<sub>0.27</sub>MnO<sub>2</sub>, ordered Na<sub>0.19</sub>MnO<sub>2</sub> and commercial MnO<sub>2</sub> materials in a 0.1 M Na<sub>2</sub>SO<sub>4</sub> electrolyte. X-ray diffraction and X-ray total scattering/PDF analyses were conducted to compare the structural difference of three materials (Figures S25-26, Tables S8-10). Our results showed that disordered Na<sub>0.27</sub>MnO<sub>2</sub> had a triclinic (C-1) birnessite structure, also supported by our neutron PDF analysis. Though disordered Na<sub>0.27</sub>MnO<sub>2</sub> and ordered Na<sub>0.19</sub>MnO<sub>2</sub> both show the birnessite layered structure, Na<sub>0.27</sub>MnO<sub>2</sub> has a smaller crystalline size and a shorter coherence length (Figure S25b) compared to Na<sub>0.19</sub>MnO<sub>2</sub>. On the other hand, commercial MnO<sub>2</sub> showed a highly crystalline and ordered β-MnO<sub>2</sub> phase. Figure S26 demonstrated the difference of local structures between disordered Na<sub>0.27</sub>MnO<sub>2</sub> and ordered Na<sub>0.19</sub>MnO<sub>2</sub> birnessite and commercial MnO<sub>2</sub>, where the former showed a more disordered lattice structure.

Figure 8b shows the CVs of disordered Na<sub>0.27</sub>MnO<sub>2</sub>, ordered Na<sub>0.19</sub>MnO<sub>2</sub> and commercial β-MnO<sub>2</sub> and a scan rate of 5 mV s<sup>-1</sup> (CVs tested at other scan rates are shown in Figure S27). Though all three materials were tested in a 2.5 V potential window, ordered Na<sub>0.19</sub>MnO<sub>2</sub> and commercial β-MnO<sub>2</sub> materials displayed obvious gas evolution features at lower and higher potential ranges. The Tafel analysis showed that disordered Na<sub>0.27</sub>MnO<sub>2</sub> displayed a much weaker HER current at potentials up to -1.25 V (equivalent to an overpotential of 0.63 V towards HER) and higher Tafel slopes at various scan rates (Figure 8c, S27), suggesting sluggish kinetics of HER compared with commercial and ordered Na-MnO<sub>2</sub> materials. It is notable that all three materials were inactive towards OER even at a potential of 1.25 V (equivalent to an overpotential of 0.63 V towards OER), however, only disordered Na<sub>0.27</sub>MnO<sub>2</sub> has high overpotential for both HER and OER, suggesting that the disordered nature leads to high resistance to the gas evolution reactions and therefore a kinetically stable potential window of 2.5 V in an aqueous electrolyte. It is worth mentioning that although ordered Na<sub>0.19</sub>MnO<sub>2</sub> and commercial β-MnO<sub>2</sub> materials showed a great capacity enhancement at a lower potential range close to -1.25 V, probably benefiting from hydrogen insertion, disordered Na<sub>0.27</sub>MnO<sub>2</sub> still showed much superior capacities at all tested scan rates. The inferior capacities from ordered Na<sub>0.19</sub>MnO<sub>2</sub> and commercial β-MnO<sub>2</sub> might be due to the parasitic gas evolution reactions especially HER that deteriorated the electrode and causes capacity loss at prolonged cycles. Previous DFT calculations demonstrated that the thermodynamically unstable edge sites of the layered transition-metal dichalcogenides nanocrystals were catalytically active for HER.<sup>47</sup> Jaramillo et al. provided direct experimental evidence showing that exchange current density of HER was proportional to the length of edges rather than the coverage area of MoS<sub>2</sub> nanoplates, and thus the edges of nanoplates were catalytically more active for HER. 57,58 However, these catalytically active sites are located on the thermodynamically unstable planes (edges of the layers), which are difficult to be exposed preferentially.<sup>59, 60</sup> In this study. disordered MnO<sub>2</sub> nanolayered structures have highly exposed (001) planes that are thermodynamically stable plane but catalytically inert, while the ordered Na<sub>0.19</sub>MnO<sub>2</sub> birnessite possesses a large grain size with a long coherent length, and therefore the edges of the layers that are thermodynamically unstable but more active toward gas evolution plane are more likely exposed.

## **Conclusions**

In this work, we have integrated detailed structural analysis with electrochemical measurements to understand the observed high capacity (up to 0.35 charge transfer per Mn atom) and good structural stability (a capacity of 89 mAh g<sup>-1</sup> after 5000 cycles) found in the disordered and Na-rich Na<sub>0.27</sub>MnO<sub>2</sub> birnessite layered materials. Through *in situ* XRD measurements, we have revealed the role of water codeintercalation with Na-ion on mitigating interlayer expansion during the high potential charging process. Investigations of solvent cointercalation properties in other layered materials will be useful and important in designing the next generation of high capacity rechargeable aqueous batteries. In addition to water trafficking, our results also manifest the promotional effects of the disordered structure on aqueous Na-ion storage: disordered Na<sub>0.27</sub>MnO<sub>2</sub> structure allows continuous and smooth structural evolution during the charging and discharging processes without phase transitions and possesses highly exposed (001) planes with low density of active edge sites for gas evolution reactions, and thus yields a large aqueous Na-ion storage capacity and long cycling life.

#### Methods

Material synthesis. Mn<sub>3</sub>O<sub>4</sub> nanoparticles were first synthesized *via* a solution phase method. In a typical synthesis, MnCl<sub>2</sub>·4H<sub>2</sub>O (0.7 g, Alfa Aesar, 99% metals basis) was fully dissolved by deionized water (140 mL, 18.2 MΩ; Millipore, Inc.) in a 500 mL flask under vigorous stirring at room temperature. The aqueous solution of NaOH (Alfa Aesar, 99.98% metals basis) with a concentration of 0.123 g mL<sup>-1</sup> was injected at a rate of 0.167 mL min<sup>-1</sup> for 50 min using an automatic syringe (HSW Inc.). After injection, the mixture continuously reacted for another 30 min till dark brown precipitate was formed. The resulting product was separated by centrifuging and then washed by deionized water and ethanol consecutively. The obtained products (Mn<sub>3</sub>O<sub>4</sub> nanoparticles) were finally vacuum-dried. In the synthesis of sodium-manganese oxides, NaOH (Alfa Aesar, 99.99% metals basis) and 100 mg Mn<sub>3</sub>O<sub>4</sub> nanoparticles were ground using a mortar and pestle with the molar ratios of 0.5, 1, 1.5, 2 and 4, respectively. The resulting mixture of NaOH and Mn<sub>3</sub>O<sub>4</sub> was heated in a tube furnace (Thermal Scientific, Inc.) in the open air at 270 °C for 6 hours. The obtained solids were thoroughly washed with deionized water to remove the possible NaOH residual and vacuumdried for overnight. Ordered Na<sub>0.19</sub>MnO<sub>2</sub> birnessite was synthesized via thermal decomposition of NaMnO<sub>4</sub> at 800 °C for 12 hours, and then washed by deionized water and ethanol, and dried in vacuum. The MnO<sub>2</sub> birnessite with low sodium concentration Na<sub>0.13</sub>MnO<sub>2</sub> was synthesized via a wet chemistry method. Aqueous MnCl<sub>2</sub> (5 mg mL<sup>-1</sup>) precursor was injected into 20 mL NaOH solution with a concentration of 5.7 mg mL<sup>-1</sup> at the rate of 0.167 mL min<sup>-1</sup> for 1 hour, and the obtained product was vacuum-dried after washed by deionized water and ethanol. And then the solids were annealed in air at 270 °C for 6 hours. The ordered MnO<sub>2</sub> birnessite was synthesized via the heating treatment of NaMnO<sub>4</sub> at a high annealing temperature at 800 °C for 12 hours, and then washed and dried overnight.

Material characterizations. Inductively coupled plasma mass spectrometry (ICP-MS) was used to identify the elemental ratios of materials. Sample aliquots were digested in mixed concentrated HCl-HNO<sub>3</sub> solution and then transferred into HNO<sub>3</sub> solution for dilution in 2% HNO<sub>3</sub> and introduction into the Nu instruments AttoM high resolution ICP-MS. Standards of known concentrations were used to correct for drift and within-instrument elemental fractionation. Triplicate runs of each sample allowed for the determination of the precision of each sample. Energy dispersive X-ray spectroscopy (EDXS) was conducted for elemental analysis by an Amray 3300FE field emission SEM with a PGT Imix-PC microanalysis system at the University of New Hampshire. Thermogravimetric analysis (TGA) was measured on a Mettler-Toledo instrument at the University of New Hampshire. Regular transmission electron microscopy (TEM) images were collected on Zeiss/LEO 922 Omega TEM at the University of New Hampshire. X-ray photoelectron spectroscopy (XPS) was measured using Thermo Scientific K-Alpha instrument at Harvard University.

#### **Electrochemical measurements.**

Half-cell test: Cyclic voltammetry (CV) measurements of sodium-manganese oxide were conducted using a three-electrode half-cell powered by CHI 660d single channel electrochemical workstation. The threeelectrode system contained a glassy carbon rotating disc electrode (Pine Instrument) as the working electrode, platinum wire and silver-silver chloride (Ag/AgCl) electrode as counter and reference electrodes, respectively. The ink material was prepared by grinding mixture of 7 mg sodium-manganese oxide and 3 mg carbon black (Alfa Aesar, > 99.9%). The resulting mixture was mixed with deionized water to make an ink solution of 0.5 mg mL<sup>-1</sup>. The resulting solution was subsequently sonicated until the materials were homogeneously dispersed. In a typical half-cell measurement, 10 µL suspension containing 3.5 µg sodiummanganese oxide and 1.5 µg carbon black was drop-cast onto the glassy carbon disc electrode (0.5 cm in diameter) and vacuum-dried. The CV measurements of electrodes were conducted in a 250 mL flat-bottom flask containing 100 mL argon-purged Na<sub>2</sub>SO<sub>4</sub> aqueous electrolyte (0.1 M) at a rotating rate of 500 rpm. The CV data were obtained within an applied potential range from -1.25 V to 1.25 V (vs Ag/AgCl) for 3 cycles, and the third CV cycle was used for the calculation of storage capacity. Na<sub>0.27</sub>MnO<sub>2</sub> was charged to 1.25 V (vs Ag/AgCl) from open circuit voltage in 0.5 M Na<sub>2</sub>SO<sub>4</sub> solution with a scan rate of 1 mV s<sup>-1</sup> by using CV in half-cell, and then discharged to -1.25 V. The charged and dischaged samples were washed and colloected for ex-situ XPS measurements.

Diffusivity measurements: The diffusivity measurements were tested in a typical half-cell setting as described above, except 40 ug active materials sodium-manganese oxides was loaded on working electrode and 0.25 M Na<sub>2</sub>SO<sub>4</sub> was used as the electrolyte. A constant negative current pulse of 1 uA was first applied to the working electrode and was held for 15 seconds to discharge the electrode from the open circuit potential. After that, the working electrode was relaxed and potential changes were collected for another 1000 seconds.

Full-cell test: Symmetric two-electrode full-cells with  $Na_{0.27}MnO_2$  electrodes were assembled and measured to characterize the energy/power performance and the long cycle stability as well. Electrodes were made by drop casting the slurry containing ~ 5 mg  $Na_{0.27}MnO_2$  and 1.25 mg carbon black as a mass ratio of 4:1 on Toray carbon paper (E-Tek, Inc., 1.5 cm in diameter). The resulting electrodes were weighed with an accurate mass loading of active material after vacuum-dried over-night. Two symmetric electrodes were separated by cellulose-based filter paper (Whatman), and 150  $\mu$ L  $Na_2SO_4$  aqueous solution (1 M) was used as the electrolyte. The cell stack of electrodes and separator were tightened by stainless plate and compression spring to ensure good electrical contact and then assembled in the split button-cells (model: EQ-STC, MTI Corp.). Galvanostatic charge and discharge measurements of symmetric full-cells were conducted on the battery analyzer (model: B-TG, Arbin Instruments) within 2.5 V potential window for 5000 cycles at the constant current densities of 1, 2, 5 and 10 A g<sup>-1</sup>. All the electrochemical calculations are provided in the supporting information. Toray paper was used as current collect for symmetric full cell measurements and stable in 2.5 V without obvious generation of hydrogen (Figure S17).

Electrochemical impedance measurements: Electrochemical impedance spectroscopy (EIS) measurements were conducted after each charge and discharge cycle in full cell at the open circuit potential with a perturbation of 5 mV and frequency range from 0.1 to 100 kHz, and the Nyquist plots were collected.

**X-ray and neutron scattering characterizations.** X-ray diffraction measurements were conducted at 17-BM-B at the Advanced Photon Source at the Argonne National Laboratory with a wavelength of  $\lambda = 0.72768$  Å. *In-situ* XRD of electrochemical half-cell measurements were conducted in a home-made cell consisted of thin carbon paper (E-Tek, Inc.) as working electrode, platinum wire and micro Ag/AgCl electrode as counter and reference electrodes, respectively. The Na<sub>2</sub>SO<sub>4</sub> aqueous electrolyte (1 M) was used as the electrolyte. The suspension of a mixture of Na<sub>0.27</sub>MnO<sub>2</sub> and carbon black was drop cast on the thin carbon paper and then dried naturally in air. The cellulose based filter paper was used as a separator. The cell was then assembled for X-ray measurements. *In-situ* XRD tests were performed during CV scans from -1.25 V to 1.25 V (vs Ag/AgCl) at the scan rates of 0.75 mV s<sup>-1</sup>. GSAS-II software was used to analyze the structural changes during the charge and discharge processes. The X-ray scattering experiment was also

conducted at 17-BM-B at the Advanced Photon Source at the Argonne National Laboratory. The total neutron scattering experiment was conducted at the Nanoscale-Ordered Materials Diffractometer (NOMAD) beamline at Spallation Neutron Source at Oak Ridge National Laboratory. The atmoic Pair Distribution Function (PDF) analysis was conducted using PDFgui software.

**Theoretical methods:** Density functional theory (DFT) calculations were performed using the WIEN2k software package, which uses full potential and linearized-augmented- planewaves with local orbitals (LAPW+ lo) to self consistently solve the Kohn-Sham equations. [61] The generalized gradient approximation of Perdew, Burke and Ernzerhof (GGA-PBE) was used for the exchange and correlation energies. [62] The plane-wave cutoff parameters  $R_{MT}K_{max}$  and  $G_{max}$  were selected as 6.5 and 12, respectively, and the cutoff energy was -6.0 Ry. The k-points of the cell was  $(1 \times 12 \times 4)$  and for the NaMnO<sub>2</sub>.H<sub>2</sub>O.

## Acknowledgments

This work was supported by the US Department of Energy (DOE), Office of Science, Basic Energy Sciences under Award # DE-SC0010286 (XT, XS, FG, DC). The research at Binghamton University is partially supported by NSF DMREF-1627583. This research used resources of the Advanced Photon Source, a US DOE Office of Science User Facility operated for the DOE Office of Science by Argonne National Laboratory under Contract No. DE-AC02-06CH11357. The Advanced Light Source is supported by the Director, Office of Science, Office of Basic Energy Sciences, of the U.S. Department of Energy under Contract No. DE-AC02-05CH11231. The neutron scattering experiments were carried out at the Spallation Neutron Source, which is sponsored by the Scientific User Facilities Division, Office of Basic Energy Sciences, US Department of Energy, under Contract No. DE-AC05-00OR22725 with Oak Ridge National Laboratory.

#### **Author contributions**

All authors contributed to the preparation of the manuscript. X.S. contributed to the material synthesis and characterizations, electrochemical experimental measurements and analysis, X-ray analysis. F.G., X.S., and D.S.C contributed to neutron PDF analysis. X.S. and W.X. contributed to X-ray measurement. Z.L.H., S. M. and L. P. contributed to XPS and DFT calculations. J.W. and W.Y. contributed to sXAS measurement and analysis. K.P., J.N., and M.F. contributed to the neutron measurements. X.S. and X.T. wrote the manuscript. X.T. contributed to the design of the experiments.

#### Additional information

**Supplementary information** accompanies this paper at http://www.nature.com

**Competing financial interests:** The authors declare no competing financial interests.

### **Materials & Correspondence**

Correspondence and requests for materials should be addressed to X.T. (xw.teng@unh.edu)

## **Reference:**

- Yabuuchi, N. *et al.* P2-type Na<sub>x</sub>[Fe<sub>1/2</sub>Mn<sub>1/2</sub>O]<sub>2</sub> made from earth-abundant elements for rechargeable Na batteries. *Nat. Mater.* **11**, 512-517, (2012).
- 2 Kim, H. et al. Aqueous Rechargeable Li and Na Ion Batteries. Chem. Rev. 114, 11788-11827, (2014).
- Wessells, C. D., Huggins, R. A. & Cui, Y. Copper hexacyanoferrate battery electrodes with long cycle life and high power. *Nat. Commun.* **2**, 5, (2011).
- Pasta, M., Wessells, C. D., Huggins, R. A. & Cui, Y. A high-rate and long cycle life aqueous electrolyte battery for grid-scale energy storage. *Nat. Commun.* **3**, 7, (2012).
- Pasta, M. *et al.* Full open-framework batteries for stationary energy storage. *Nat. Commun.* **5**, 9, (2014).
- Pasta, M. *et al.* Manganese-cobalt hexacyanoferrate cathodes for sodium-ion batteries. *J. Mater. Chem. A* **4**, 4211-4223, (2016).
- Wang, L. *et al.* A superior low-cost cathode for a Na-ion battery. *Angew. Chem. Int. Ed.* **52**, 1964-1967, (2013).
- Song, J. *et al.* Removal of Interstitial H2O in Hexacyanometallates for a Superior Cathode of a Sodium-Ion Battery. *J. Am. Chem. Soc.* **137**, 2658-2664, (2015).
- 9 Lu, Y. H., Wang, L., Cheng, J. G. & Goodenough, J. B. Prussian blue: a new framework of electrode materials for sodium batteries. *Chem. Commun.* **48**, 6544-6546, (2012).
- Billaud, J. *et al.* beta-NaMnO2: A High-Performance Cathode for Sodium-Ion Batteries. *J. Am. Chem. Soc.* **136**, 17243-17248, (2014).
- 11 Caballero, A. *et al.* Synthesis and characterization of high-temperature hexagonal P2-Na0.6MnO2 and its electrochemical behaviour as cathode in sodium cells. *J. Mater. Chem.* **12**, 1142-1147, (2002).
- 12 Clement, R. J., Bruce, P. G. & Grey, C. P. Review- Manganese-based P2-type transition metal oxides as sodium-ion battery cathode materials. *J. Electrochem. Soc.* **162**, A2589-A2604, (2015).
- Delmas, C., Fouassier, C. & Hagenmuller, P. STRUCTURAL CLASSIFICATION AND PROPERTIES OF THE LAYERED OXIDES. *Physica B & C* **99**, 81-85, (1980).
- 14 Mendiboure, A., Delmas, C. & Hagenmuller, P. ELECTROCHEMICAL INTERCALATION AND DEINTERCALATION OF NAXMNO2 BRONZES. *J. Solid State Chem.* **57**, 323-331, (1985).
- Doeff, M. M., Peng, M. Y., Ma, Y. P. & Dejonghe, L. C. ORTHORHOMBIC NAXMNO2 AS A CATHODE MATERIAL FOR SECONDARY SODIUM AND LITHIUM POLYMER BATTERIES. *J. Electrochem. Soc.* **141**, L145-L147, (1994).
- Kim, S., Ma, X. H., Ong, S. P. & Ceder, G. A comparison of destabilization mechanisms of the layered NaxMO2 and LixMO2 compounds upon alkali de-intercalation. *Phys. Chem. Chem. Phys.* **14**, 15571-15578, (2012).
- 17 Li, X. *et al.* Jahn-teller assisted Na diffusion for high performance Na ion batteries. *Chem. Mat.* **28**, 6575-6583, (2016).
- Tian, M., Gao, Y. R., Wang, Z. X. & Chen, L. Q. Understanding structural stability of monoclinic LiMnO2 and NaMnO2 upon de-intercalation. *Phys. Chem. Chem. Phys.* **18**, 17345-17350, (2016).
- 19 Choi, Y. & Liu, P. Understanding of ethanol decomposition on Rh(111) from density functional theory and kinetic Monte Carlo simulations. *Catalysis Today* **165**, 64-70, (2011).
- Yeager, M. *et al.* Highly efficient K<sub>0.15</sub>MnO<sub>2</sub> birnessite nanosheets for stable pseudocapacitive cathodes. *J. Phy. Chem. C* **116**, 20173-20181, (2012).
- Qu, Q. et al. Electrochemical performance of MnO<sub>2</sub> nanorods in neutral aqueous electrolytes as a cathode for asymmetric supercapacitors. J. Phy. Chem. C 113, 14020-14027, (2009).

- Wang, J., Zhang, G. & Zhang, P. Layered birnessite-type MnO2 with surface pits for enhanced catalytic formaldehyde oxidation activity. *J. Mater. Chem. A* **5**, 5719-5725, (2017).
- Zhu, H. T. *et al.* Birnessite-type MnO<sub>2</sub> nanowalls and their magnetic properties. *J. Phy. Chem. C* **112**, 17089-17094, (2008).
- Cai, J., Liu, J. & Suib, S. L. Preparative Parameters and Framework Dopant Effects in the Synthesis of Layer-Structure Birnessite by Air Oxidation. *Chem. Mat.* **14**, 2071-2077, (2002).
- Brousse, T., Toupin, M. & Belanger, D. A hybrid activated carbon-manganese dioxide capacitor using a mild aqueous electrolyte. *J. Electrochem. Soc.* **151**, A614-A622, (2004).
- Athouel, L. *et al.* Variation of the MnO2 birnessite structure upon charge/discharge in an electrochemical supercapacitor electrode in aqueous Na2SO4 electrolyte. *J. Phys. Chem. C* **112**, 7270-7277, (2008).
- Liu, Y. *et al.* High-performance aqueous sodium-ion batteries with K0.27MnO2 cathode and their sodium storage mechanism. *Nano Energy* **5**, 97-104, (2014).
- Suo, L. M. *et al.* "Water-in-salt" electrolyte enables high-voltage aqueous lithium-ion chemistries. *Science* **350**, 938-943, (2015).
- 29 Xu, K. & Wang, C. S. Widening voltage windows. *Nat. Energy* **1**, 2, (2016).
- Yamada, Y. *et al.* Hydrate-melt electrolytes for high-energy-density aqueous batteries. *Nat. Energy* **1**, 9, (2016).
- Peng, L. *et al.* Ultrathin Two-Dimensional MnO2/Graphene Hybrid Nanostructures for High-Performance, Flexible Planar Supercapacitors. *Nano Letters* **13**, 2151-2157, (2013).
- Yeager, M. P. *et al.* Pseudocapacitive Hausmannite Nanoparticles with (101) Facets: Synthesis, Characterization, and Charge-Transfer Mechanism. *ChemSusChem* **6**, 1983-1992, (2013).
- Chen, R., Zavalij, P. & Whittingham, M. S. Hydrothermal Synthesis and Characterization of KxMnO2·yH2O. *Chem. Mat.* **8**, 1275-1280, (1996).
- Park, Y. J. & Doeff, M. A. Synthesis and electrochemical characterization of M2Mn3O8 (M=Ca, Cu) compounds and derivatives. *Solid State Ion.* **177**, 893-900, (2006).
- Liu, T. C., Pell, W. G., Conway, B. E. & Roberson, S. L. Behavior of Molybdenum Nitrides as Materials for Electrochemical Capacitors: Comparison with Ruthenium Oxide. *J. Electrochem. Soc.* **145**, 1882-1888, (1998).
- Nagasubramanian, G., Jungst, R. G. & Doughty, D. H. Impedance, power, energy, and pulse performance characteristics of small commercial Li-ion cells. *J. Power Sources* **83**, 193-203, (1999).
- Wu, Z.-S. *et al.* High-Energy MnO2 Nanowire/Graphene and Graphene Asymmetric Electrochemical Capacitors. *ACS Nano* **4**, 5835-5842, (2010).
- He, Y. *et al.* Freestanding Three-Dimensional Graphene/MnO2 Composite Networks As Ultralight and Flexible Supercapacitor Electrodes. *ACS Nano* **7**, 174-182, (2013).
- Zhang, D., Zhang, Y., Luo, Y. & Chu, P. K. Highly porous honeycomb manganese oxide@carbon fibers core—shell nanocables for flexible supercapacitors. *Nano Energy* **13**, 47-57, (2015).
- Li, Z., Young, D., Xiang, K., Carter, W. C. & Chiang, Y.-M. Towards high power high energy aqueous sodium-ion batteries: The NaTi<sub>2</sub>(PO<sub>4</sub>)<sub>3</sub>/Na<sub>0.44</sub>MnO<sub>2</sub> system. *Adv. Energy Mater.* **3**, 290-294, (2013).
- Hou, Z., Li, X., Liang, J., Zhu, Y. & Qian, Y. An aqueous rechargeable sodium ion battery based on a NaMnO2-NaTi2(PO4)3 hybrid system for stationary energy storage. *J. Mater. Chem. A* **3**, 1400-1404, (2015).
- Brousse, T. *et al.* Long-term cycling behavior of asymmetric activated carbon/MnO2 aqueous electrochemical supercapacitor. *Journal of Power Sources* **173**, 633-641, (2007).
- Shan, X. Q. *et al.* Bivalence Mn5O8 with hydroxylated interphase for high-voltage aqueous sodium-ion storage. *Nat. Commun.* **7**, 8, (2016).

- Yu, X. & Manthiram, A. Performance Enhancement and Mechanistic Studies of Room-Temperature Sodium–Sulfur Batteries with a Carbon-Coated Functional Nafion Separator and a Na2S/Activated Carbon Nanofiber Cathode. *Chem. Mat.* **28**, 896-905, (2016).
- Zheng, J., Yan, P., Kan, W. H., Wang, C. & Manthiram, A. A Spinel-Integrated P2-Type Layered Composite: High-Rate Cathode for Sodium-Ion Batteries. *J. Electrochem. Soc.* **163**, A584-A591, (2016).
- Kang, B. & Ceder, G. Battery materials for ultrafast charging and discharging. *Nature* **458**, 190-193, (2009).
- 47 Radin, M. D. *et al.* Narrowing the Gap between Theoretical and Practical Capacities in Li-Ion Layered Oxide Cathode Materials. *Adv. Energy Mater.* **7**, (2017).
- 48 Li, W., Asl, H. Y., Xie, Q. & Manthiram, A. Collapse of LiNi1—x—yCoxMnyO2 Lattice at Deep Charge Irrespective of Nickel Content in Lithium-Ion Batteries. *J. Am. Chem. Soc.* **141**, 5097-5101, (2019).
- Kondrakov, A. O. *et al.* Charge-Transfer-Induced Lattice Collapse in Ni-Rich NCM Cathode Materials during Delithiation. *J. Phys. Chem. C* **121**, 24381-24388, (2017).
- Grenier, A. *et al.* Reaction Heterogeneity in LiNi0.8Co0.15Al0.05O2 Induced by Surface Layer. *Chem. Mat.* **29**, 7345-7352, (2017).
- Scofield, J. H. Theoretical Photoionization Cross Sections from 1 to 1500 keV. *Lawrence Livermore Laboratory, U.S. Atomic Energy Commission,* (1973).
- 52 Spahr, M. E., Novák, P., Haas, O. & Nesper, R. Electrochemical insertion of lithium, sodium, and magnesium in molybdenum(VI) oxide. *Journal of Power Sources* **54**, 346-351, (1995).
- Levi, E., Gofer, Y. & Aurbach, D. On the Way to Rechargeable Mg Batteries: The Challenge of New Cathode Materials. *Chemistry of Materials* **22**, 860-868, (2010).
- Sai Gautam, G., Canepa, P., Richards, W. D., Malik, R. & Ceder, G. Role of Structural H2O in Intercalation Electrodes: The Case of Mg in Nanocrystalline Xerogel-V2O5. *Nano Letters* **16**, 2426-2431, (2016).
- Lim, S. Y. *et al.* Lattice Water for the Enhanced Performance of Amorphous Iron Phosphate in Sodium-Ion Batteries. *ACS Energy Letters* **2**, 998-1004, (2017).
- Nam, K. W. *et al.* Critical Role of Crystal Water for a Layered Cathode Material in Sodium Ion Batteries. *Chemistry of Materials* **27**, 3721-3725, (2015).
- Hinnemann, B. *et al.* Biomimetic Hydrogen Evolution: MoS2 Nanoparticles as Catalyst for Hydrogen Evolution. *J. Am. Chem. Soc.* **127**, 5308-5309, (2005).
- Jaramillo, T. F. *et al.* Identification of Active Edge Sites for Electrochemical H<sub>2</sub> Evolution from MoS<sub>2</sub> Nanocatalysts. *Science* **317**, 100-102, (2007).
- Kong, D. *et al.* Synthesis of MoS2 and MoSe2 Films with Vertically Aligned Layers. *Nano Letters* **13**, 1341-1347, (2013).
- Kibsgaard, J., Chen, Z., Reinecke, B. N. & Jaramillo, T. F. Engineering the surface structure of MoS2 to preferentially expose active edge sites for electrocatalysis. *Nat. Mater.* **11**, 963, (2012).
- Schwarz, K., & Blaha, P. Solid state calculations using WIEN2k. Computational Materials *Science* **28**, 259-273, (2003).
- Perdew, J. P., Burke, K. & Ernzerhof, M. Generalized gradient approximation made simple. *Phys. Rev. Lett.* **77**, 3865 (1996)

## **Figures**

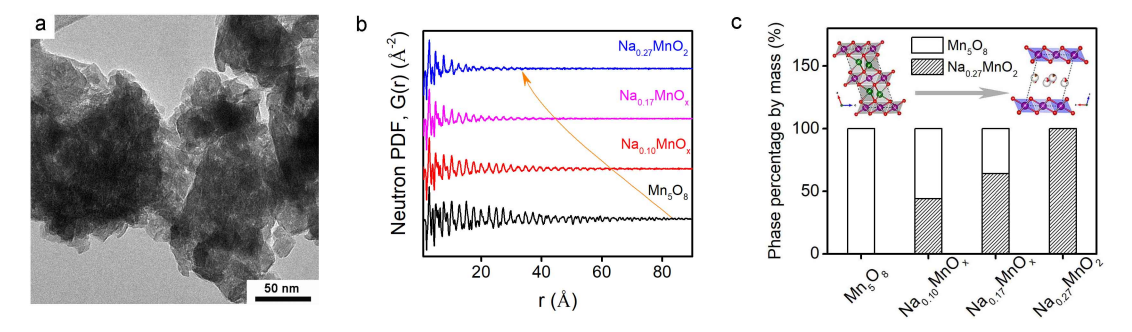


**Figure 1.** (a) TEM image of of Na<sub>0.27</sub>MnO<sub>2</sub> materials; (b) Experimental neutron PDFs of Na<sub>δ</sub>MnO<sub>x</sub> materials, where coherent lengths, defined as the longest interatomic distance of the material, decreased as the Na concentration increased; (c) Phase percentage of Na<sub>0.27</sub>MnO<sub>2</sub> in Na<sub>δ</sub>MnO<sub>x</sub> materials obtained from neutron PDF analysis.

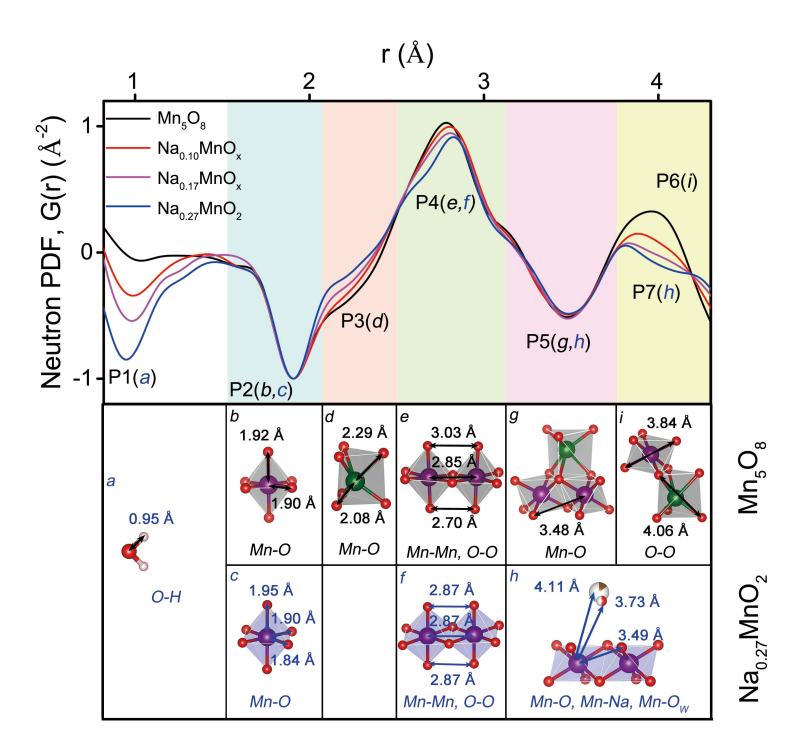


**Figure 2.** Neutron PDFs of  $Na_\delta MnO_x$  materials normalized by the intensity of the peak at 1.9 Å associated with Mn-O pair of  $Mn^{4+}$  octahedral units. The atom pair associated with each peak (P1 to P7) can be attributed to (a) water, (b, d, e, g, i)  $Mn_5O_8$  polyhedra in black and (c, f, h)  $MnO_2$  polyhedra in blue.

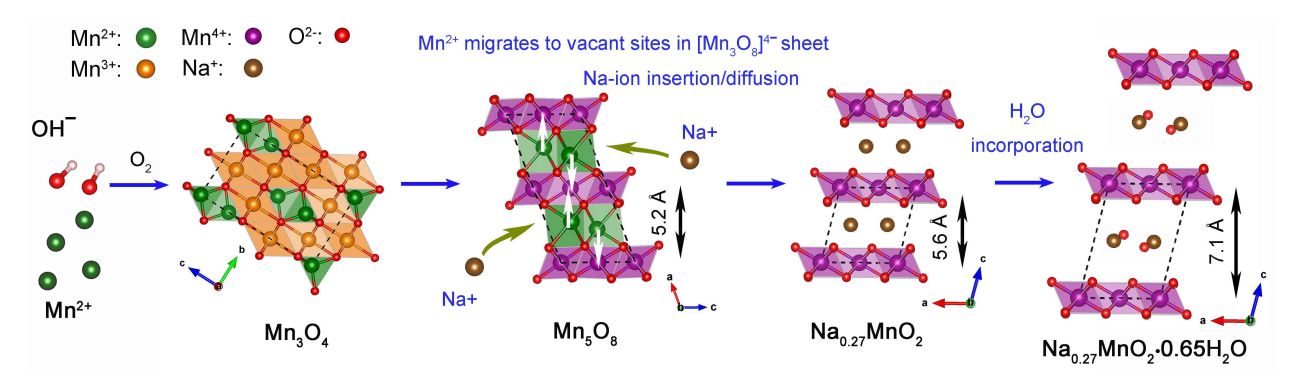


**Figure 3.** The proposed formation mechanism for  $Na_{0.27}MnO_2 \cdot 0.65H_2O$  driven by solid-state Na-ion intercalation in  $(Mn^{2^+}$ : green;  $Mn^{3^+}$ : orange;  $Mn^{4^+}$ : purple;  $Na^+$ : brown; O: red).

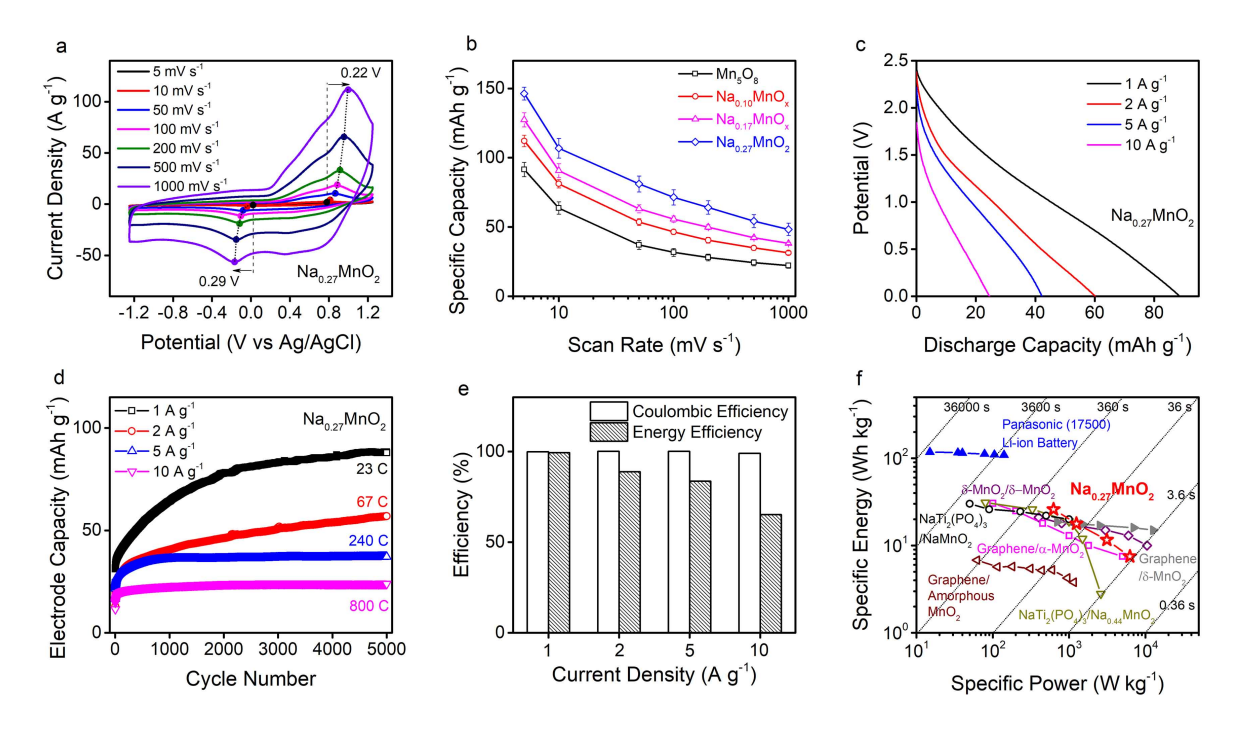


**Figure 4.** Electrochemical half-cell measurements with (a) Cyclic Voltammetry (CV) scans of Na<sub>0.27</sub>MnO<sub>2</sub> material between -1.25 V to 1.25 V (vs Ag/AgCl) at various scan rates in 0.1 M Na<sub>2</sub>SO<sub>4</sub> electrolyte; (b) calculated specific charge storage capacities of sodium-manganese oxides as a function of scan rates; Symmetric full-cell measurements with (c) discharge electrode capacities of Na<sub>0.27</sub>MnO<sub>2</sub> material at the various current densities of 1 A g<sup>-1</sup>, 2 A g<sup>-1</sup>, 5 A g<sup>-1</sup> and 10 A g<sup>-1</sup> (after 5000 galvonstatic charge and discharge process unless specified otherwise); (d) electrode capacites of Na<sub>0.27</sub>MnO<sub>2</sub> as a function of cycle number up to 5000 at the current densities from 1 A g<sup>-1</sup> to 10 A g<sup>-1</sup>; (e) coulombic and energy efficiencies of Na<sub>0.27</sub>MnO<sub>2</sub> at various current densities as a function of current density (1, 2, 5 and 10 A g<sup>-1</sup>); (f) Ragone plot with gravimetric specific energy and power of the symmetric Na<sub>0.27</sub>MnO<sub>2</sub> full–cell after 5000 galvanostatic cycles. The aqueous (empty symbols) and non–aqueous (solid symbols) devices are reported, and the gravimetric specific energy and power are calculated by the mass of electrode materials except the Panasonic (17500) Li–ion batteries.

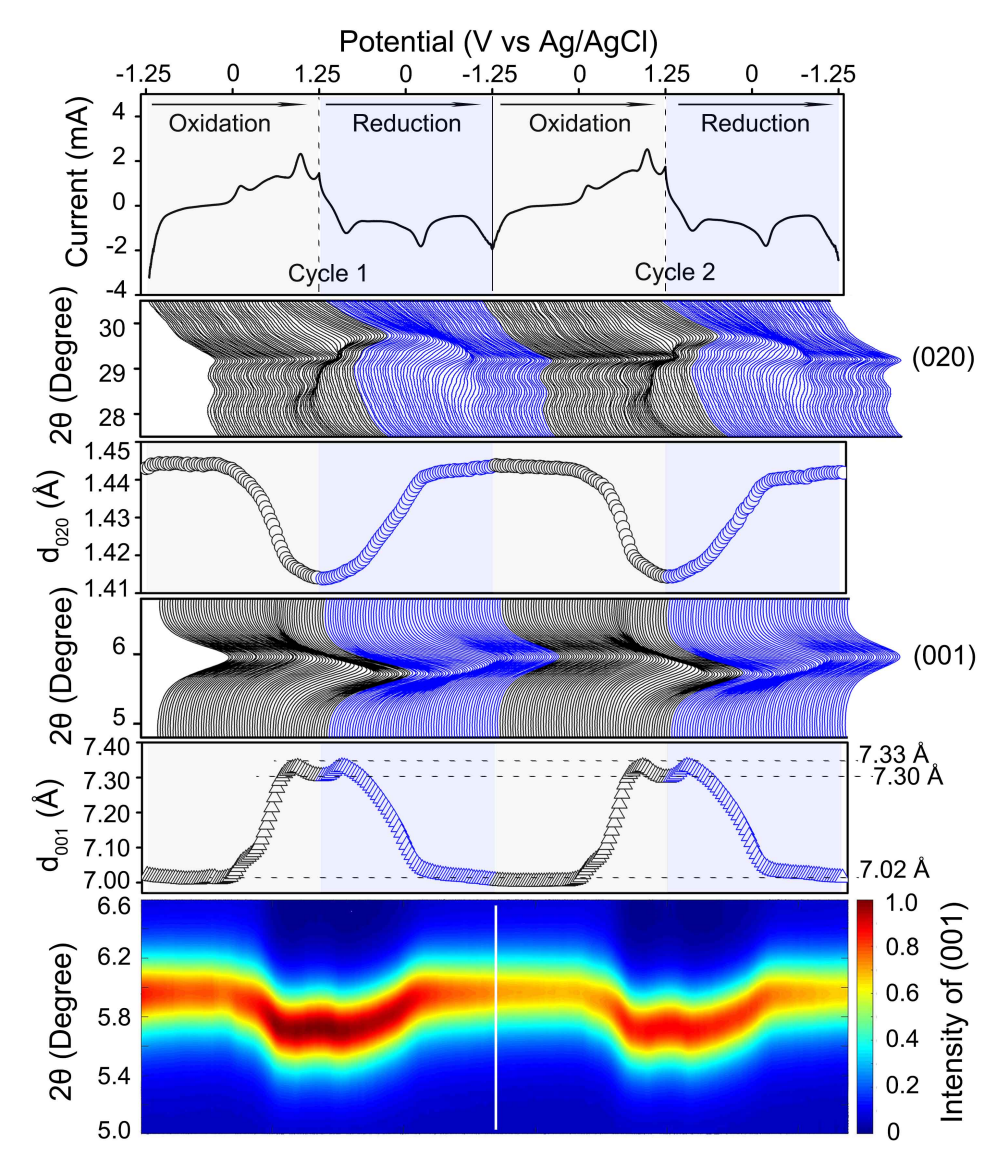


**Figure 5**. *In–situ* XRD characterization of Na<sub>0.27</sub>MnO<sub>2</sub> during two CV scans between –1.25 V and 1.25 V at a scan rate of 0.75 mV s<sup>-1</sup>, showing the changes of d–spacing for (001) basal diffraction plane and (020) Bragg diffraction plane and the contour plot peak variation of (001) plane during the charging (black) and discharging (blue) processes.

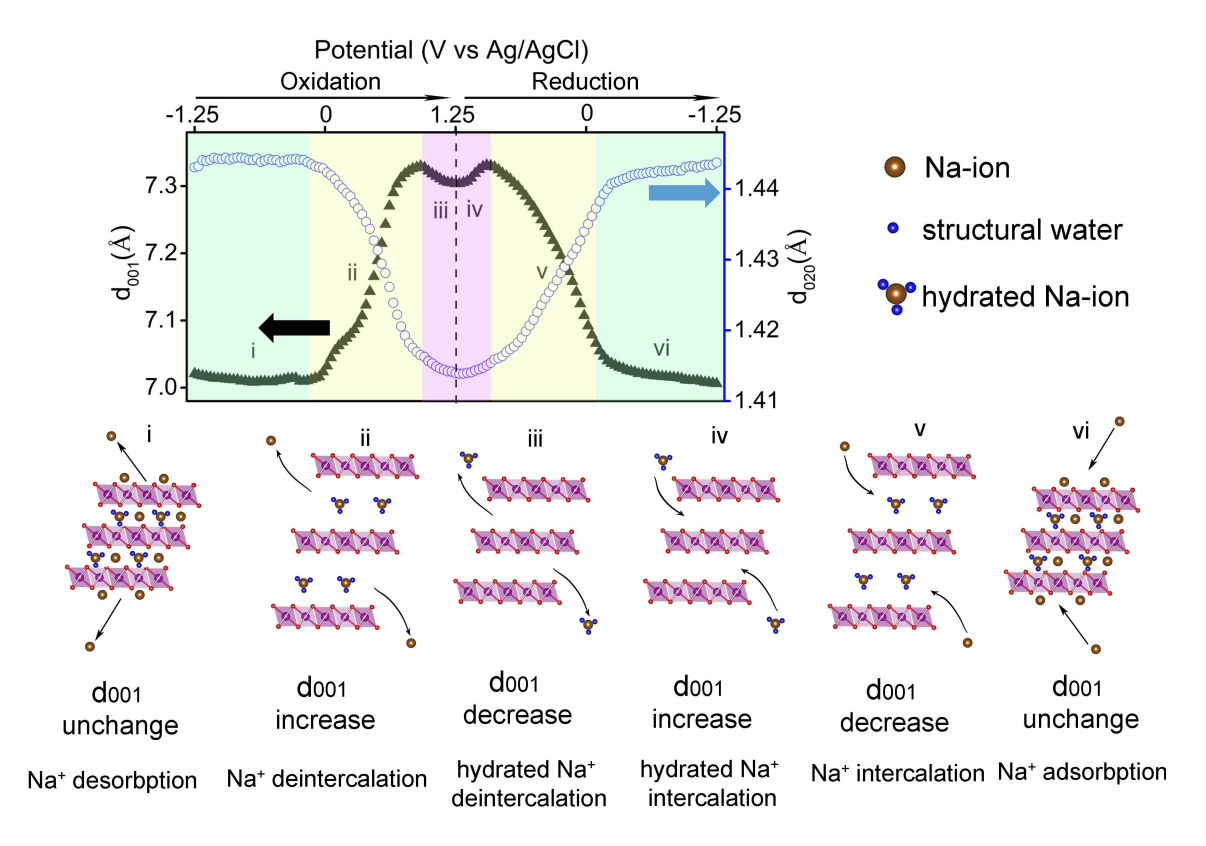


**Figure 6.** Schematic of Na-ions and water co-de intercalation and co-intercalation within the interlayer region of the Na<sub>0.27</sub>MnO<sub>2</sub> during charging (oxidation) and discharging (reduction) processes.

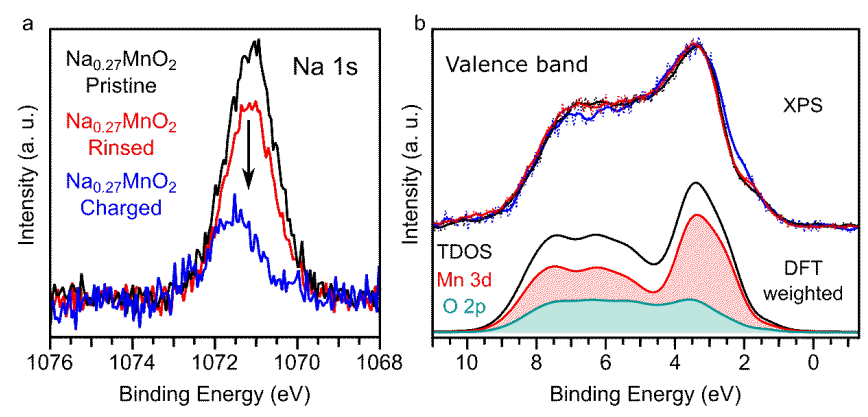


**Figure 7:** XPS measurements of the (a) Na 1s region for pristine Na<sub>0.27</sub>MnO<sub>2</sub> powder, Na<sub>0.27</sub>MnO<sub>2</sub> powder rinsed in the Na<sub>2</sub>SO<sub>4</sub> electrolyte, and (b) valence band of Na<sub>0.27</sub>MnO<sub>2</sub> electrode charged to 1.25 V (vs Ag/AgCl). The valence band XPS spectra are compared with DFT calculations of the TDOS and the Mn 3d and O 2p PDOS for the Na<sub>0.27</sub>MnO<sub>2</sub> system.

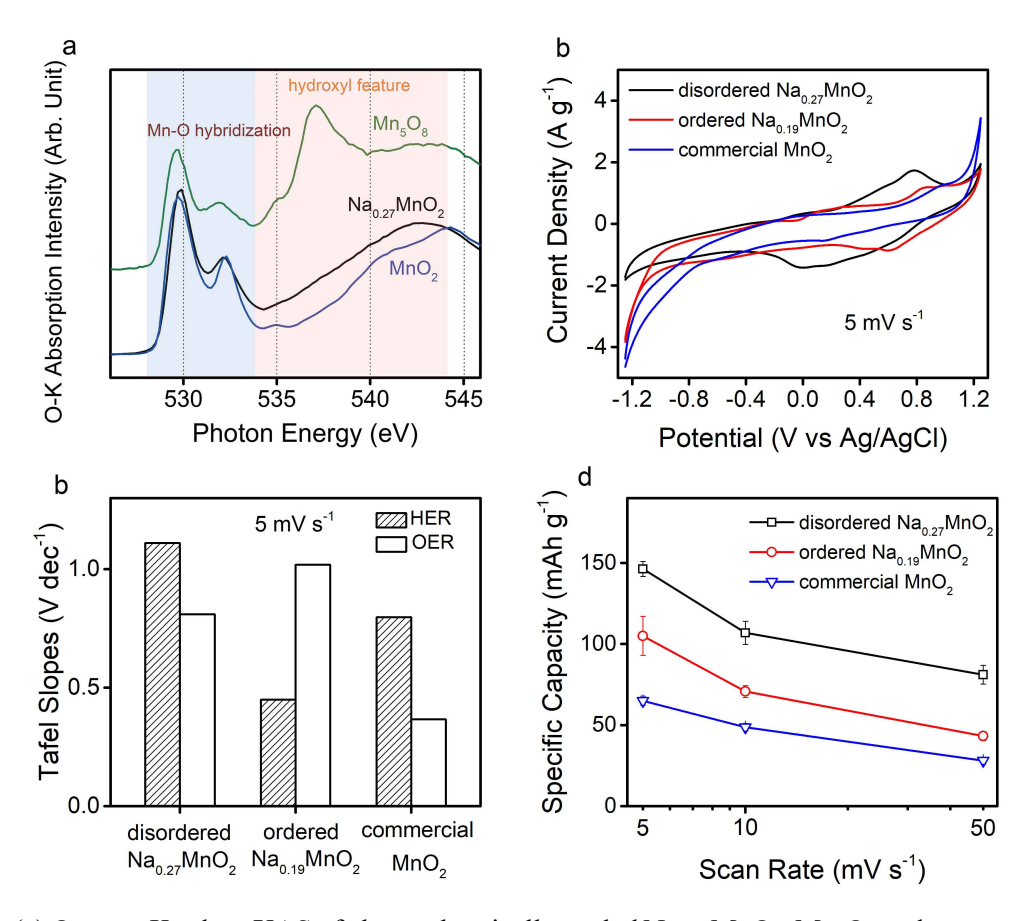


**Figure 8.** (a) Oxygen K-edge sXAS of electrochemically cycled Na<sub>0.27</sub>MnO<sub>2</sub>, Mn<sub>5</sub>O<sub>8</sub> and commercial MnO<sub>2</sub> materials; (b) CV scans of disordered Na<sub>0.27</sub>MnO<sub>2</sub>, ordered Na<sub>0.19</sub>MnO<sub>2</sub> and commercial MnO<sub>2</sub> materials at the scan rate of 5 mV s<sup>-1</sup> in a 2.5 V potential window in half-cell; (c) calculated Tafel slopes of HER and OER at the scan rate of 5 mV s<sup>-1</sup>; (d) Specific capacities at the scan rate of 5, 10 and 50 mV s<sup>-1</sup>;